Microstructure and properties of steady magnetic field-assisted laser welded joints of CP780-TRIP590 steels

Xiaoou Zhu[1]*, Zhanqi Liu[1], Fufa Wu[1], Guili Yin[1], Minghua Chen[1], Yan Zhang[2]

[1] *1. School of Materials Science and Engineering, Liaoning University of Technology, Jinzhou, 121001 Liaoning, P. R. China*
[2] *Harbin Welding Training Institute, Harbin, 2310027 Heilongjiang, P. R. China*

Abstract

Tailored blank laser welding was performed on dissimilar automobile metals, i.e., CP780 and TRIP590 steels, by coupling laser welding with a steady-state magnetic field. Before magnetic field application, the weld seam center was mainly composed of proeutectoid ferrite, acicular ferrite, granular bainite, and upper bainite, whereas the heat-affected zone on both sides was mainly composed of lath martensite and lower bainite. Under the same heat-input conditions, magnetic field application makes the laser energy more concentrated and accelerates the crystallization process of the weld pool, reducing the width of welded joints. Therefore, lath martensite and lower bainite are generated in the weld seam center, and only martensite is generated in the heat-affected zone, while the grain size in the heat-affected zone on both sides is reduced. Under a heat input of $160 \, \text{J} \, \text{mm}^{-1}$, the comprehensive mechanical properties of the welded joints exhibit the most significant improvement with a magnetic induction intensity of 20 mT.

1. Introduction

Due to its energy saving, emission reduction, and environmental protection advantages, "automobile lightweight" has become a research hotspot in automotive scientific and technological innovations [1]. For lightweight automotive materials and structures, some advanced high-strength steels, such as complex phase (CP), transformation-induced plasticity (TRIP), and dual phase (DP) steels, have been widely applied to replace common steels in vehicle body manufacturing [2–4]. Fiber laser has many merits, including excellent beam quality, high brightness, high power, deep penetrability, and low beam divergence [5, 6]; thus, it has gradually become an important welding technique and process in automobile manufacturing.

TRIP and CP steels are widely used in the automobile manufacturing industry due to their excellent mechanical properties. TRIP steels have a "Trans-formation Induced Plasticity" effect, excellent tensile strength, and a high strain hardening index, and their microstructure is a poly-phase mixture of ferrite, residual austenite, and bainite. On the other hand, the microstructure of CP steels is composed of a ferritic or bainite matrix, and pearlite, bainite, and martensite are distributed in the matrix. The strength of CP steel plates can be enhanced by the precipitation and strengthening effects of bainite or other precipitates. Currently, the microstructure and properties of laser welded joints of TRIP and CP steels have attracted extensive attention from scholars.

As regards TRIP steels, Švec et al. [7] conducted fiber laser welding tests on TRIP 690T steel plates and HSLA LAD340 steel plates with different thicknesses under a power of 3600 W and a welding speed of $70 \, \text{mm} \, \text{s}^{-1}$. They reported that the microstructure of the weld seam zone was composed of martensite, lower bainite, and a small amount of upper bainite, while the fine-grained zone near the TRIP690T steel con-

*Corresponding author: e-mail address: clzxo@lnut.edu.cn

sisted of martensite, lower bainite, and ferrite. In the critical temperature interval, the proportion of ferrite increased as the distance from the weld seam center increased. The conclusions confirm the TRIP steels microstructural constituents and mechanical properties, which can be compared with several previous works [8–13]. As regards CP steels, there are only a few recent experimental studies on laser welding technology. P. Švec et al. [14] conducted a butt-joint welding test using a fiber laser on DP980 and CP780 steels with a thickness of 1.5 mm. Under a laser power of 3900 W and a welding speed of 70 mm s^{-1}, the microstructure of the weld seam zone was composed of martensite and lower bainite, while in the coarse crystal zones on both sides of the joint, the presence of lath martensite and a small amount of lower bainite was observed. The tensile strength of the welded joint ranged between 823–826 MPa. The conclusions confirm the CP steels microstructural constituents and can be compared with several previous works [15–18].

According to existing studies, the mechanical properties and weld seam microstructure of the welded joints of TRIP and CP steels are mainly affected by the chemical composition of the base metal, plate thickness, and welding parameters (e.g., welding power and welding speed) [14, 17, 18]. With the increase of the heat input, the martensite proportion in the weld seam zone gradually decreases, and the width of the heat-affected zone gradually increases. Currently, the laser welding technology of dissimilar automotive advanced high-strength steels mainly focuses on the welding process of TRIP-DP steels [19, 20] and CP-DP steels [14]. Nevertheless, attention is seldom paid to the welding process of dissimilar metals of TRIP and CP steels. Nowadays, TRIP and CP steels are both used in the production and manufacture of automobile body structures, and there are indispensable demands and possibilities as regards the connection of dissimilar steels. Hence, there is a certain significance and value in studying the laser welding process of these two materials.

Laser welding has the advantages of high energy density, good welding quality, and small deformation. Nevertheless, due to the poor stability of the laser welding process, the fluid flow in the molten welding pool is vigorous, which can affect the weld forming process and the microstructure and properties of the welded joints [21]. In view of this, several researchers have attempted to apply a magnetic field to the laser welding process of nonmagnetic metal materials such as aluminum alloys and stainless steel. It has been found that the magnetic field has a significant effect on the molten pool flow of laser welding. Hence, to improve the microstructure and properties of welded joints, appropriate magnetic field parameters need to be selected [22–27]. Therefore, it is particularly important to analyze the microstructure and properties of welded joints and optimize the welding process parameters by conducting laser welding tests on dissimilar advanced high-strength automotive steels (i.e., TRIP and CP steels) with the application of the magnetic field. Thus, it is of significance to improve automobile safety performance, broaden the applications of high-strength steels, and reduce the use amount of vehicle body materials.

Herein, TRIP590 and CP780 steels are used as the research materials, and a steady-state magnetic field is applied to the tailored blank laser welding process of dissimilar automotive high-strength steels. The synergistic effects of the steady-state magnetic field and the heat input on the macroscopic morphology, microstructure, hardness, and tensile properties of the welded joints are explored, and the laser welding process parameters for the welding of automotive high-strength steels are optimized. It is believed that the present work can broaden the application range of magnetic field-assisted laser welding technology and provide theoretical and practical references for lightweight automobile research.

2. Materials and methods

2.1. Materials

The materials used in the following experiments were CP780 high-strength steel and TRIP590 steel produced by Shanghai Baosteel Group, China; the supply status was a cold rolled state. The micro-constituents are typical of TRIP and CP steels, as reported by Švec and Wang et al. [7, 8, 14]. The microstructure of the TRIP590 steel containing twin crystals exists around the ferrite grains, which is confirmed as retained austenite by SAED analysis. Moreover, the martensite structure with high-density dislocation morphology is confirmed by SAED analysis. Their microstructure is shown in Fig. 1a.

The microstructure of CP780 steel is shown in Fig. 1b. Acicular carbides distributed in parallel in a small part of ferrite are characterized as lower bainite structure, and the black striped structure of martensite is confirmed by the SAED analysis. The dimensions of the test materials are 55 mm × 60 mm × 1 mm. The alloy elements and mechanical properties of the two materials are listed in Tables 1 and 2, respectively.

2.2. Methods

In the tailored blank laser welding process of dissimilar metals, i.e., CP780 steel and TRIP590 steel, in this study, the process parameters with the greatest impact on joint performance are the laser power, welding speed, and defocus amount. Although most scholars usually select high laser welding power in their

Ta b l e 1. Alloy elements' maximal concentration of TRIP590 and CP780 steels (wt.%)

Material	C	Si	Mn	Cr	P	S	Al	Fe
TRIP590	0.17	2.0	2.0	0.06	0.01	0.005	2.0	Bal.
CP780	0.18	0.8	2.2	1.0	0.08	0.015	2.0	Bal.

Ta b l e 2. Mechanical properties of TRIP590 and CP780 steels

	Yield strength (MPa)	Tensile strength (MPa)	Hardness, HV	Elongation (%)
TRIP590	380 (minimal)	620 (minimal)	187 (average)	28 (minimal)
CP780	500 (minimal)	790 (minimal)	238 (average)	10 (minimal)
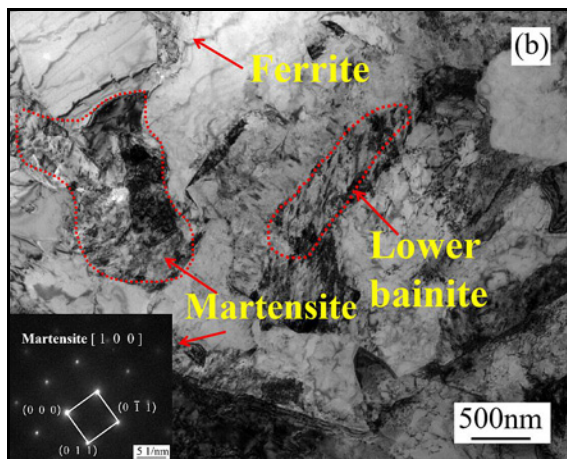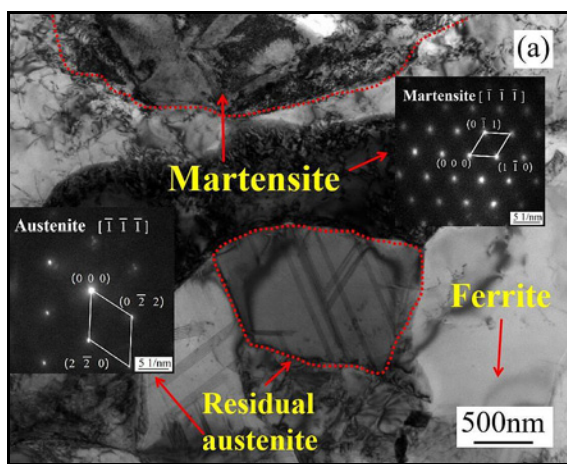
Fig. 1. Microstructure of base materials: (a) TEM image of TRIP590 steel and (b) TEM image of CP780 steel.

Fig. 2. Schematic diagram of welding experiment.

experiments [7–20], it is equally important to investigate the laser welding process under low power when considering the production and manufacturing costs. In the tailored blank laser welding tests, a G1080L-1000W fiber laser produced by China Guoyao Laser Company was used as the heat source and Ar as the protective gas. Before welding, the surface of the test plates was polished with a series of sandpapers, and then, the parts to be welded were cleaned with acetone. Both sides of the two test plates were fixed with stainless-steel fixtures on a stainless-steel workbench, and the welding joint form was butt-joint. To explore the effect of the applied magnetic field on the microstructure and properties of the welded joints of dissimilar metals, a NdFeB strong permanent magnet with a surface magnetic induction intensity of 150 mT was fixed horizontally under the original stainless-steel fixture. The dimensions of the permanent magnet were 60 mm × 20 mm × 5 mm, as presented in Fig. 2.

In the experiment, the magnetic induction value was altered by adjusting the distance between the permanent magnet and the surface of the plates to be welded. In general, the closer the vertical distance between the permanent magnet and the surface of the plates to be welded, the higher the magnetic induction intensity at their surface. The axis of the permanent magnet along the length direction coincided with the joint gap, and the front and back ends of the permanent magnet were flush with the head and tail ends of the welding direction of the test plate. This way, the magnetic induction lines through each position of the joint gap of the test plates to be welded were all upright, and the received magnetic field induction in-

Table 3. Welding parameters of the joints

Group number	Laser power (W)	B (mT)	Welding speed (mm s^{-1})	Heat input (J mm^{-1})	Gas-flow rate (L min^{-1})	Defocus amount (mm)	Seam gap (mm)	Spot diameter (mm)
1	500	0		100				
2		20						
3	600	0		120				
4		20	5		15	0	0.5	1.0
5	700	0		140				
6		20						
7	800	0		160				
8		20						

tensity values were approximately the same. A liquid crystal display HT201 high-precision Gauss meter was utilized to measure the magnetic induction intensity at the welding gap position during the experiment. The measured value was displayed by a digital voltmeter in the instrument. The measuring accuracy could reach 0.1 mT with a relative error of 2.0 %.

Before welding, the vertical distance between the permanent magnet and the bottom of the test plate to be welded was set to 43 mm. First, along the starting position of the welding direction of the test plate, the magnetic induction intensity values along the vertically upward direction at the surface of the joint gap of the test plate to be welded were measured at an interval of 5 mm. It was found that the vertically upward magnetic field induction intensity values at all points on the surface were basically the same along the welding direction. The deviation between the measured values was between +1.8 and –2.0 mT, and the average magnetic induction intensity value at the surface of the joint gap of the plate to be welded was found to be about 20.0 mT. According to the above measurement method, when the vertical distance between the permanent magnet and the bottom of the plate to be welded was set to 35 mm, the magnetic induction intensity at the surface of the joint gap of the plate to be welded was about 30.0 mT; when the vertical distance was 31 mm, the magnetic induction intensity was about 40.0 mT.

To explore the synergistic effect of the magnetic field and the heat input on the microstructure and properties of the welded joints, four different heat inputs were selected. Under each heat input value, two sets of tests were conducted; in the first, no magnetic field was applied; in the second, a certain magnetic field was applied. All remaining process parameters and pre-welding preparation processes were consistent. Equation (1) was used to calculate the heat input:

$$\text{Heat input} = P/V, \tag{1}$$

where P (W) is laser power and V (mm s^{-1}) is welding speed.

Subsequently, eight groups of laser welding tests were conducted along the rolling direction of the base material; the process parameters are listed in Table 3.

After welding, metallographic samples were prepared from the welded joints by wire cutting. The bulk samples cut from the joints were ground and polished by a series of sandpapers and then etched with a 5 % nitric acid solution. Immediately after, the macroscopic morphology was observed by a Zeiss Stemi508 stereomicroscope. Subsequently, the weld seams were polished and etched with 4 % nitrate alcohol solution, and their microstructure and heat-affected zones on both sides were observed by a Zeiss SIGMA 500 field-emission scanning electron microscope (FESEM). The samples of two types of base metals, the weld center and the coarse-grained areas on both sides before and after adding the magnetic field, were prepared by double-jet electrolytic thinning. Moreover, the microstructure of the samples was identified by a Tecnai G2 T20 transmission electron microscope. Then, hardness tests were performed at the central position of the welded joints every 0.1 mm along the horizontal direction using an HVS-10 automatic Vickers hardness tester. The loading pressure was 200 gf, and the pressure holding time was 10 s. Tensile strength tests were conducted by a Metes CMT5305 electronic universal testing machine on the eight groups of tensile specimens prepared with different welding parameters. The thickness of all specimens was 1 mm. The surface of the weld seams was polished, and then the specimens were machined into tensile specimens according to the ASTM E8-2016 standard; their dimensions are shown in Fig. 3. After tensile testing, the average values of the tensile strength, yield strength, and elongation of each group of specimens were determined. Finally, the tensile fracture morphologies of the eight groups of welded joints were observed by FESEM.

T a b l e 4. Macro-morphology of the surface of welded joints under 160 J mm^{-1}

Position	B = 0 mT	B = 20 mT
Front surface		
Bottom surface		
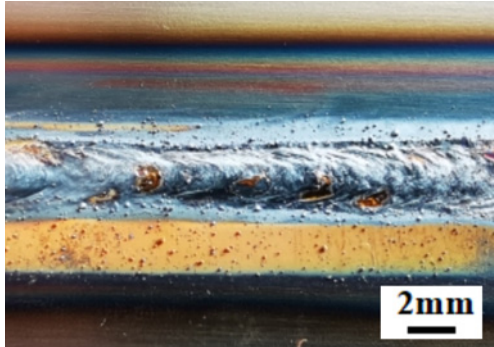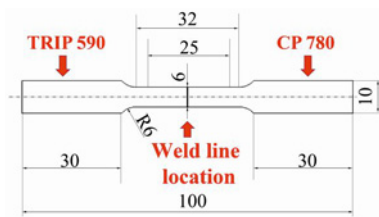
Fig. 3. Schematic diagram of the tensile samples.
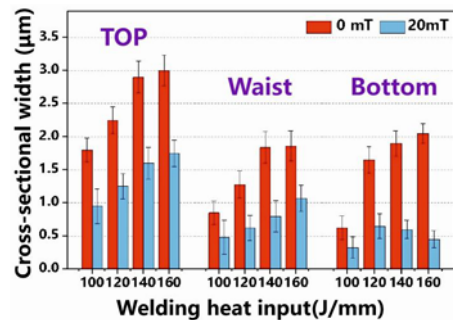
Fig. 4. Cross-sectional widths of the top, waist, and bottom portions at the weld seam.

3. Results and discussion

3.1. Macroscopic morphology of welded joints

After welding, no obvious defects, such as cracks or incomplete welding, were observed on the surface of the eight groups of welded joints. The local macroscopic morphologies of the joints without surface processing are presented in Table 4.

By comparing the table in parallel, it can be found that under a heat input of 160 J mm^{-1}, joint forming is relatively poor before magnetic field application, while there is an obvious splash. After magnetic field application, the width of the weld seam is significantly reduced, and the widths of the weld seam surface and the heat-affected zone, as well as the splash phenomenon, decrease significantly. These findings indicate that the magnetic field has a positive promot-

ing effect on laser welding energy concentration and forming.

Subsequently, the widths of the top, waist, and bottom portions of the weld cross-section in all eight groups of welded joints were measured, and the results are presented in Fig. 4. Without magnetic field application, the widths of the top, waist, and bottom portions of the weld cross-section increase with increasing heat input level.

Overall, under the same heat input level, when a magnetic field with a magnetic induction intensity of 20 mT is applied, the widths of the weld seams at the top, waist, and bottom portions are all significantly reduced compared to those without a magnetic field
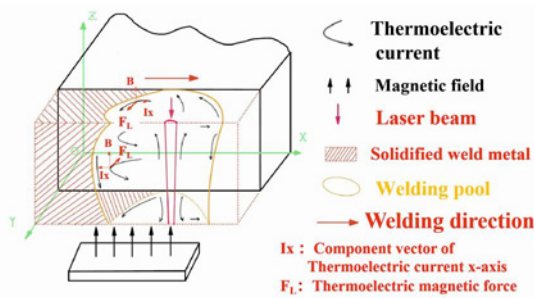
Fig. 5. Interaction between the magnetic field and weld pool.

application. These test results are mainly attributed to the effect of the auxiliary magnetic field on the weld molten pool flow.

In the laser welding process assisted by a steady-state magnetic field, the current in the molten pool originates mainly from two aspects, and accordingly, the force generated by the steady-state magnetic field has two different effects on the molten weld pool.

The first is the Hartmann effect; that is, the conductive fluid in the molten pool is affected by the magnetic field, forming an induced current and simultaneously producing a Lorentz force. The Lorentz force direction is always opposite to the flow direction of the melt and can inhibit the flow of the melt [28–33]. Usually, a Hartmann coefficient Ha^2 is used to characterize the inhibitory effect of the magnetic field on the melt, which is defined as follows:

$$Ha^2 = \sigma B^2 L^2/\eta, \qquad (2)$$

where L is the half-width of the weld seam, σ is the electrical conductivity, B is the magnetic field intensity, and η is the dynamic viscosity.

According to Bachmann et al. [30, 33], as regards magnetic materials, when the magnetic induction intensity B is about $500\,mT$, and the weld width is about $7\,mm$, i.e., when the Hartmann coefficient Ha^2 is about 10^4, the external magnetic field can have an apparent inhibitory effect on the molten pool. The value of B is known ($20\,mT$), and the width of the weld seam is about 2–$3\,mm$. Assuming that σ and η have no significant changes in the order of magnitude, by equal proportional conversion, the value of Ha^2 is between 1.31 and 3.1, which is much smaller than 10^4 [34]. Consequently, the magnetic induction resistance is far from adequate to compensate for the viscous force and, thus, far from enough to exert an inhibitory effect on the molten pool. Hence, in this study, the influence of the Hartmann effect on the molten pool is ignored.

The second is the Seebeck effect; that is, during the laser welding process, a thermal current can be pro-

duced between the front zone of the liquid phase region and the solid zone in the molten pool. Most scholars believe that the current in the molten pool in the welding process mainly originates from the thermal current caused by the temperature gradient [35–40]. When a magnetic field is applied, the thermal current can produce a thermoelectric magnetic force under the effect of the magnetic field in its movement process, which can drive the local flow of the molten pool. Figure 5 illustrates the interaction between the thermoelectric magnetic force and the welding pool. The direction of the magnetic induction lines (B) is perpendicular to the X-O-Y horizontal plane. Moreover, it is vertically upward and parallel to the Z-axis. The thermal current I flows mainly in the X-O-Z plane [41], which generates an I_x component parallel to the X-axis and an I_z component parallel to the Z-axis. Since $I_z \parallel B$, the thermal current component I_z along the Z-direction does not interact with the vertical magnetic induction line B. Since the magnetic induction line B passes vertically through the thermal current I_x, according to Fleming's left-hand rule, a thermoelectric magnetic force F_L parallel to the Y-axis can be generated at the thermal current I_x in the molten pool under the action of the vertically upward magnetic field. Therefore, the thermoelectric magnetic force F_L can drive the local convection at the center of the molten pool, thus accelerating the crystallization process and significantly reducing the molten pool volume. Under the condition of a certain temperature and magnetic induction intensity, F_L satisfies the following:

$$F_L \propto \sigma \Delta T B, \qquad (3)$$

where F_L is the thermoelectric magnetic force, σ is the electrical conductivity of the melt, S is the absolute electric potential energy, ΔT is the temperature gradient, and B is the magnetic induction intensity [42].

It is not difficult to realize that, with the increase of the laser heat input level, the molten pool temperature keeps increasing, which can lead to the decrease of the temperature gradient ΔT, the decrease of the electrical conductivity σ, and the decrease of the absolute electric potential energy S. As a result, the thermoelectric magnetic force F_L keeps decreasing, and its action force on the molten pool decreases gradually as well. Under the same magnetic induction intensity, the volume of the weld seams increases gradually with increasing heat input level. On the other hand, along with the increase of the heat input level, the existence time of the molten pool is prolonged. Consequently, the existence time of the thermoelectric magnetic stirring effect on the melt flow is prolonged accordingly, which can cause obvious changes to the internal flow direction in the molten pool, resulting in an energy decrease at its bottom portion [40].
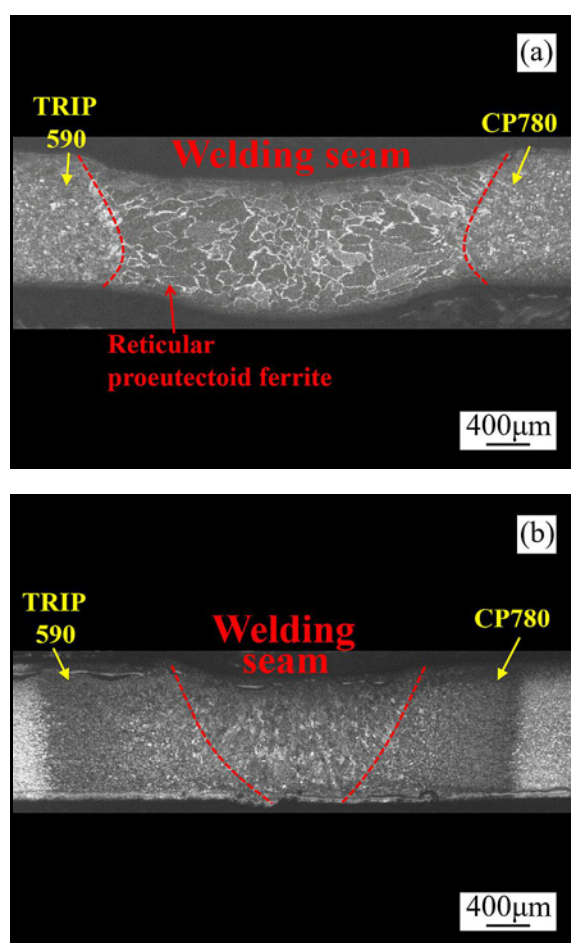
Fig. 6. Overall micro-morphology of the weld seam: (a) 160 J mm^{-1}-0 mT and (b) 160 J mm^{-1}-20 mT.

Hence, under the action of thermoelectric magnetic force, the cross-sectional widths of all groups were significantly shortened. In particular, when the heat input level was 160 J mm^{-1}, i.e., maximum heat input, there was a root hump defect at the bottom of the weld. After magnetic field application, it was found that the root hump defect disappeared. The above test results are consistent with the analysis in Table 6 and Fig. 5.

3.2. Weld seam center microstructure

Figure 6 shows the overall microstructure at the weld seam center in the welded joints. As it can be observed, under no magnetic field application, a lot of reticular pre-eutectoid ferrites exist in the weld seam center. After the magnetic field is applied, the electromagnetic force can disturb the crystallization direction of the weld seam metal; thus, the growing pre-eutectoid ferrite grains are continuously scoured, resulting in reticular grain reduction. The magnetic field application promotes the proliferation of dendrites, drives the convection of the local melt [34], and finally

affects the changes in the weld seam structure.

Before magnetic field application, due to the low heat input (30–80 J mm^{-1}) selected by previous authors [7–16], the cooling rate was high, and the microstructure of the weld seam center during the laser welding of the TRIP590 and CP780 steels was dominated by lath martensite and lower bainite. However, the heat input selected in the present study is high, i.e., within the range of 100–160 J mm^{-1}. Consequently, no martensite structure could be found in the center of the weld seam.

Figure 7a displays the microstructure of the weld seam center under a heat input of 160 J mm^{-1} before magnetic field application. Since the heat input is the highest and the residence time at high temperatures is the longest, the temperature gradient is the lowest, and the overall grain size is the largest.

When the welded metal gradually cools from the high temperature, the proeutectoid ferrite precipitates at the grain boundaries of the original austenite in the high-temperature region during the $\gamma \to \alpha$ phase transition. The morphology of the proeutectoid ferrite precipitated at the grain boundaries is variational. A certain amount presents an elongated-strip shape along the grain boundaries, and the remaining amount presents a morphology of connected polygons distributed along the grain boundaries [43–45], as shown in Fig. 7a.

Some granular bainite with relatively fine grain boundaries (ferrite and island-like carbon-rich austenite) is found at the grain boundaries, which consists of "ferrite + island structure". The islands in the granular structure are irregularly shaped and distributed on the ferrite matrix, as shown in Figs. 7a,b. The island-like particles in the granular bainite are found to be relatively small, which is conducive to improving the plastic toughness of the weld seam [43, 44].

During the $\gamma \to \alpha$ phase transition in the medium-temperature region, a large amount of small cross-distributed acicular ferrite is formed, and the direction difference between two adjacent ferrite particles presents a large dip angle (60°–90°), which is the main microconstituent in the weld center conducive to improving the weld seam strength, as shown in Figs. 7a,c.

With the decrease of the temperature, it can be found that a few particles are distributed among the parallel elongated lath ferrites precipitated at the preeutectoid ferrites, which exhibit a feathered shape. As verified by Refs. [7, 45], this is a brittle and hard upper bainite, as shown in Fig. 7a.

The SEM and TEM microstructure of the weld seam center under a heat input of 160 J mm^{-1} after magnetic field application is exhibited in Figs. 7d,e.

Due to the high cooling rate, a large amount of parallel lath microscopic structure is generated inside the original austenite grains, as shown in Fig. 7d. According to TEM, black stripe structures with high dis-
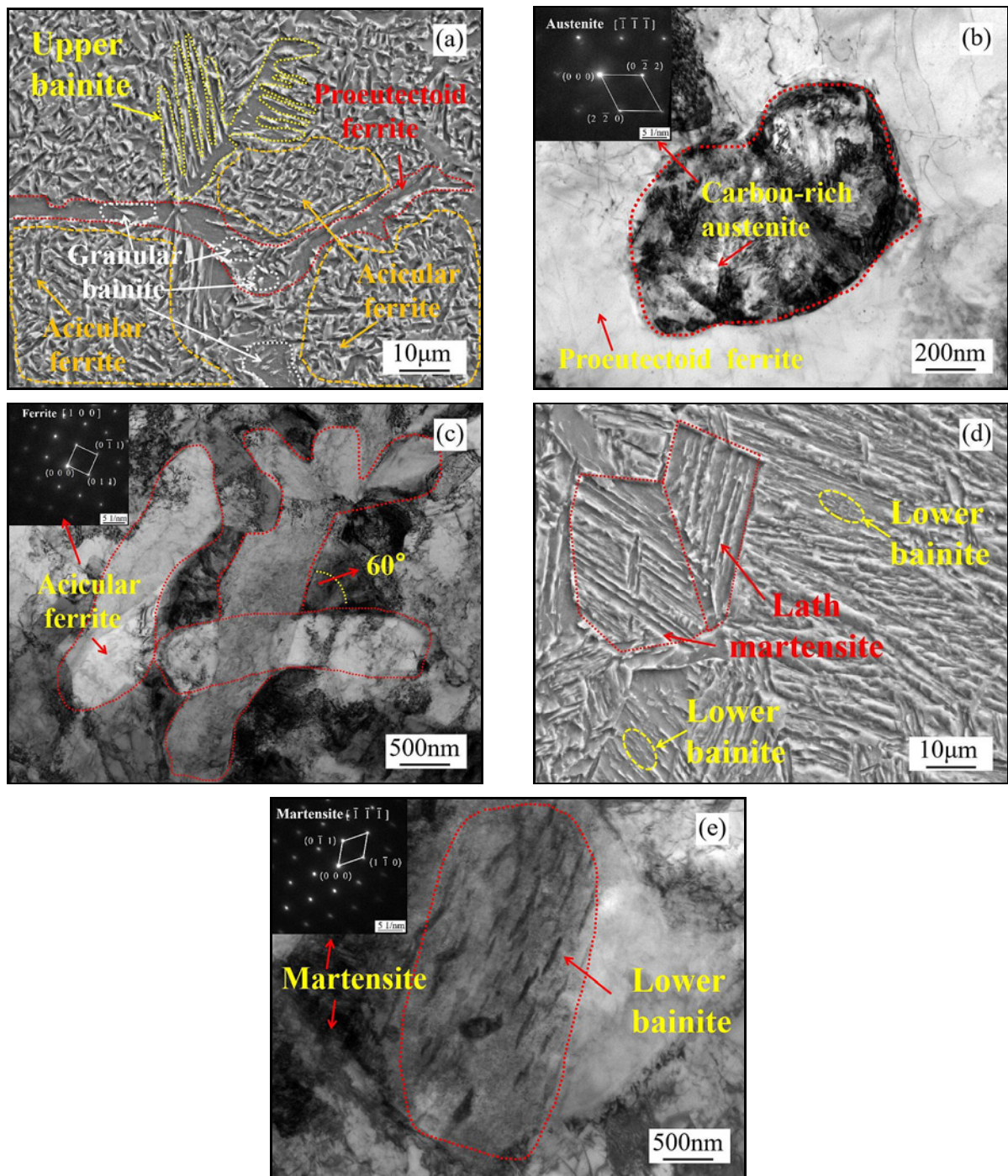
Fig. 7. Microstructure in the center of weld seam: (a) SEM image of 160 J mm^{-1}-0 mT, (b) TEM image of 160 J mm^{-1}-0 mT (granular bainite), (c) TEM image of 160 J mm^{-1}-0 mT (acicular ferrite), (d) SEM image of 160 J mm^{-1}-20 mT, and (e) TEM image of 160 J mm^{-1}-20 mT (lath martensite and lower bainite).

location density can be found near the grain boundary of the original austenite and carbides distributed in rows inside the ferrite, as shown in Fig. 7e. According to the relevant literature [7, 8, 10, 13, 16] and SAED analysis, it is confirmed that the microstructure of the weld seam center is composed of lath martensite and lower bainite. These martensitic lath bundles and lower bainite are generated inside the original coarse austenitic bulk grain structure due to the stirring effect of the thermoelectric magnetic force, which promotes the solid phase transition under the rapid cooling condition of the molten pool [10, 13]. Hence, within a certain heat input range, the application of a magnetic field can significantly improve the weld seam microstructure of dissimilar metals, i.e., TRIP590-CP780 steel.

3.3. Microstructure of the heat-affected zone of welded joints

Due to the similar content of alloy elements in TRIP590 and CP780 steels, the microstructures of their heat-affected zone are similar. When the tempe- rature of the heat-affected zone of the TRIP590 and CP780 steels reaches the highest peak temperature above the critical transition temperature of A_{c3}, the grains grow up rapidly after complete austenitization, and coarse grain structures can be formed near the fused boundaries.
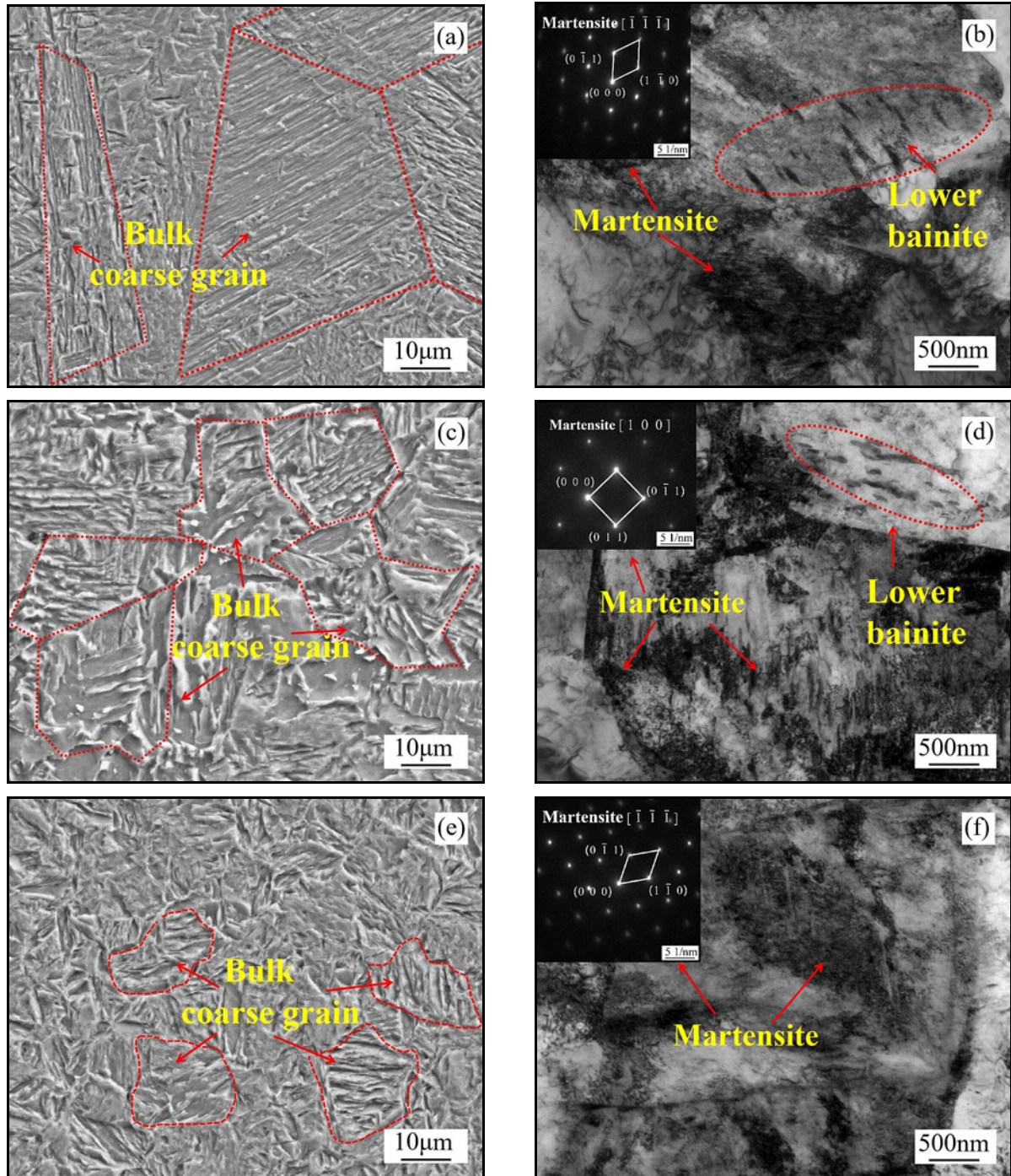
Fig. 8a–f. Microstructure of coarse grain zone in the heat-affected zone: (a) SEM image of 160 J mm^{-1}-0 mT (TRIP590 side), (b) TEM image of 160 J mm^{-1}-0 mT (TRIP590 side), (c) SEM image of 160 J mm^{-1}-0 mT (CP780 side), (d) TEM image of 160 J mm^{-1}-0 mT (CP780 side), (e) SEM image of 160 J mm^{-1}-20 mT (TRIP590 side), and (f) TEM image of 160 J mm^{-1}-20 mT (TRIP590 side).
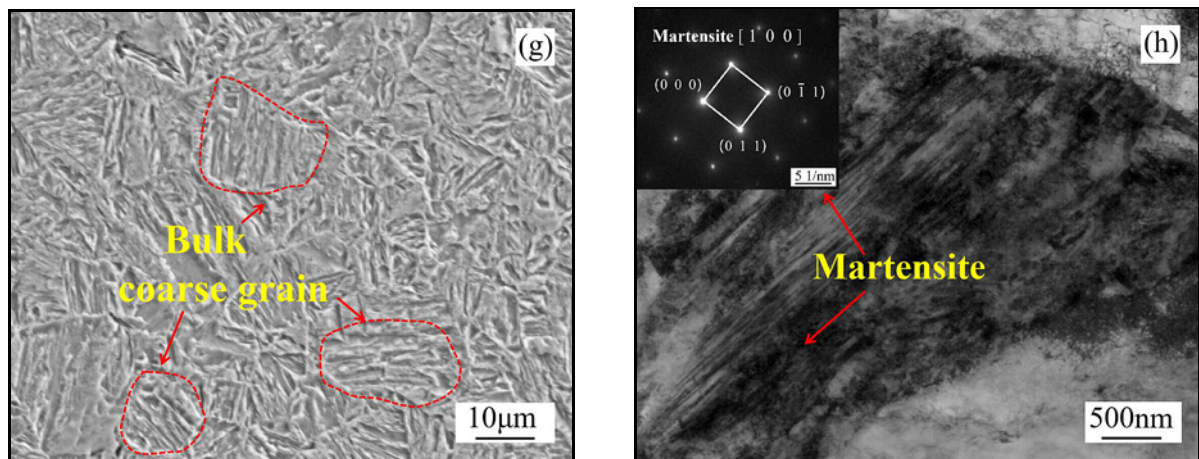
Fig. 8g,h. Microstructure of coarse grain zone in the heat-affected zone: (g) SEM image of 160 J mm^{-1}-20 mT (CP780 side) and (h) TEM image of 160 J mm^{-1}-20 mT (CP780 side).

With the increase of the heat input, the coarse-grain structure remains above the A_{c3} line for a longer time, and the grain size of the coarse-grain zone on both sides of the joint increases. Figures 8a–d depict the microstructure of the coarse-grain zones on the TRIP590 and CP780 steel sides, respectively, under a heat input of 160 J mm^{-1} before magnetic field application.

On the TRIP590 steel side, the severe grain growth in the coarse-grain zones and the increased austenitic homogenization degree enhance the quenching hardening tendency. In Fig. 8a, completely austenitized grains can be observed with a coarser grain size ranging from 50–100 μm. Due to the coarse grain in this region, the heat-affected zone has higher hardness and lower plasticity, which is the weak link of the welded joints with poor comprehensive mechanical properties.

On the CP780 steel side, due to the low quenching tendency and relatively small grain size of the base material, the grains grow up rapidly after complete re-austenitization, and their size ranges within 30–60 μm. Compared to the TRIP590 steel, the coarsening degree of the heat-affected zone near the CP780 steel is smaller, as shown in Fig. 8c. In the rapid cooling process after welding, the microstructure possesses high hardness.

By comparison to previous research results [7, 14, 46, 47] and according to TEM images in Figs. 8b,d and SAED analysis, it is confirmed that the microstructure of the coarse-grain zones on both sides is dominated by lath martensite and a small amount of lower bainite. The identification criteria of these microstructures are consistent with those shown in Figs. 1 and 7.

After magnetic field application under a heat input of 160 J mm^{-1}, the microstructures of the coarse-grain zones on the TRIP590 and CP780 steel sides are exhibited in Figs. 8e-8h.

By comparing Figs. 8a,e and Figs. 8c,f, it can be found that, after magnetic field application, the resi-dence time of the coarse-grain zones remaining above the A_{c3} line becomes shorter, hindering the growth of austenitized grains. Here, the size of the grains in the coarse-grain zone on the TRIP590 steel side ranges within 20–30 μm, and that of those on the CP780 steel side within 10–20 μm, as shown in Figs. 8e,g. Due to the cooling rate acceleration, the coarsening degree of the coarse-grain zones on both sides is decreased. The direction difference of the parallel stripped bundles in adjacent bulk coarse grain exhibits a large dip angle, leading to a decrease in the embrittlement tendency of the coarse grains, which improves the comprehensive mechanical properties of the welded joint.

The microstructures of HAZ coarse grain areas on both sides of the magnetic-field-assisted laser joint are observed by TEM and SAED analysis. Only martensite is found, and no lower bainite structure is observed, as shown in Figs. 8f and 8h. The identification criteria of these microstructures are consistent with those shown in Figs. 1 and 7.

3.4. Mechanical properties of welded joints

Figure 9 illustrates the hardness distribution diagram of the welded joints in Groups 1–8. As can be observed, the hardness distribution trends of the welded joints in the eight groups are roughly the same. The hardness at the weld seam is relatively low, while that of the heat-affected zone near the weld seam on the side of the TRIP590 steel is relatively high, which gradually decreases towards the base metal. On the side of the CP780 steel, there are different degrees of softening in the heat-affected zone, and the softening degree can be expressed by the softening ratio r, as defined in Eq. (4):

$$r = H_{\min}/H_{BM}, \qquad (4)$$

where $H_{\min}$ is the minimal micro-hardness in the heat-
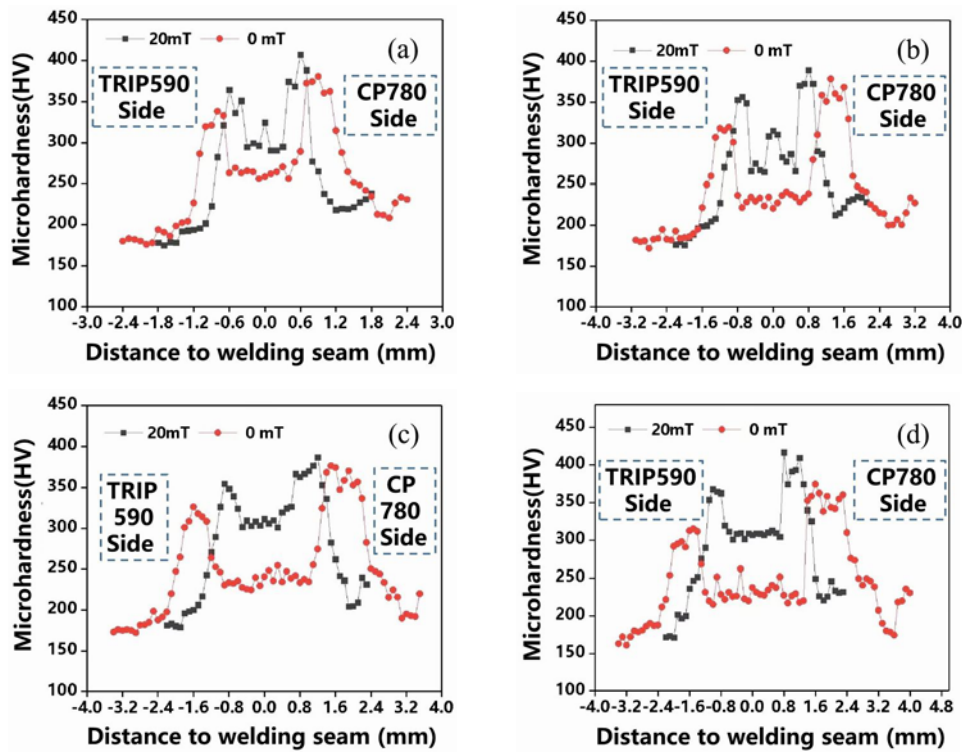
Fig. 9. Micro-hardness of welded joint: (a) $100 \, \mathrm{J \, mm^{-1}}$, (b) $120 \, \mathrm{J \, mm^{-1}}$, (c) $140 \, \mathrm{J \, mm^{-1}}$, and (d) $160 \, \mathrm{J \, mm^{-1}}$.
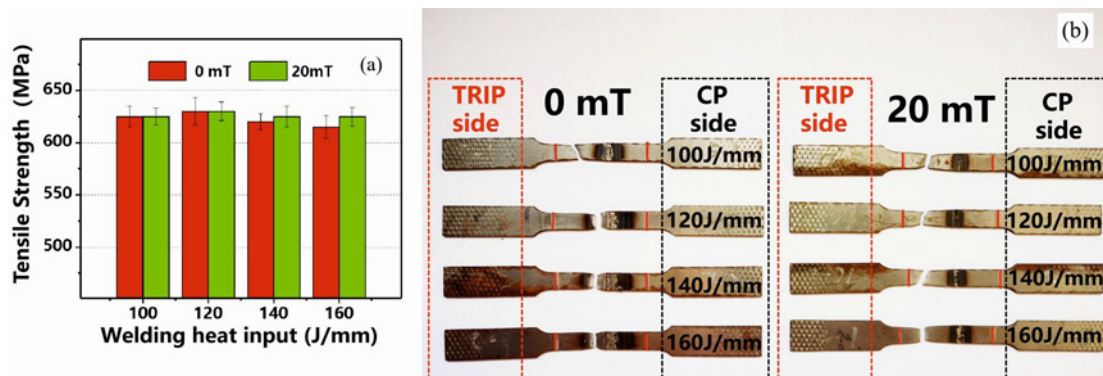
Fig. 10. Results of tensile test of welded joints: (a) tensile strength and (b) fracture position.

-affected zone on the side of the CP780 steel and H_{BM} is the average micro-hardness on the CP780 steel base metal (238HV).

When the heat input increases from 100 to $160 \, \mathrm{J \, mm^{-1}}$ and before magnetic field application, the softening ratios of the heat-affected zone on the side of the CP780 steel are 0.88, 0.84, 0.81, and 0.73. After magnetic field application, the softening ratios are 0.92, 0.89, 0.86, and 0.93, respectively, and the softening phenomenon is relieved. At the same time, the average hardness values of the weld seam also increase by 12.24, 19.18, 32.66, and 33.27 %, respectively.

To sum up, before magnetic field application, the hardness of the weld seam center decreases gradually with increasing heat input level, and the softening phe-

nomenon is gradually aggravated. The time subjected to electromagnetic stirring in the molten pool expands gradually with increasing heat input level, which promotes the expansion of the region where the martensitic structure is formed. Due to the decrease of the grain size and the shortening of the heat-affected zone width on the side of the CP780 steel, the softening degree can be decreased significantly. These results show that the effect of magnetic field application on joint hardening is significant.

The tensile properties of the welded joints in Groups 1–8 were tested, and the results are presented in Fig. 10. As it can be observed in Fig. 10a, before magnetic field application, the tensile strength of dissimilar metal welded joints is similar to that of
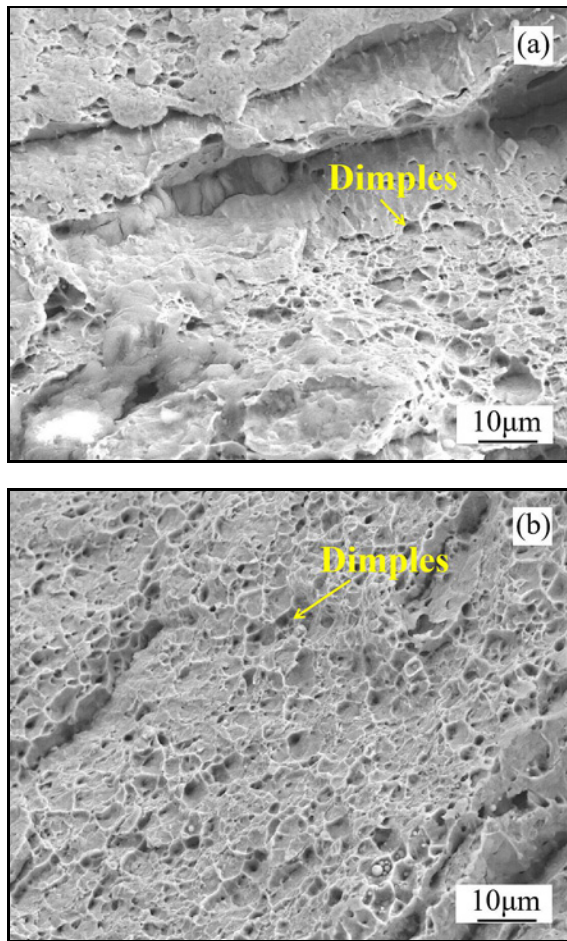
Fig. 11. Fracture morphology of tensile specimen of joint: (a) 160 J mm^{-1}-0 mT and (b) 160 J mm^{-1}-20 mT.

the TRIP590 steel base metal (620.0 MPa). However, when no magnetic field is applied, with the increase of the heat input, the embrittlement phenomenon of the coarse crystals in the coarse-grain zone on the TRIP590 steel side is aggravated. Consequently, the joints prepared within the heat input range of 120–160 J mm^{-1} are all fractured in the coarse-grain zone on the TRIP590 steel side (Fig. 10b). After magnetic field application, the cooling rate on the TRIP590 steel side is accelerated due to the concentration of laser energy, resulting in a fine-grain strengthening phenomenon of the microstructure in the coarse-grain zone. Consequently, the fracture positions of the four groups of joints are all located at the base metal near the heat-affected zone on the TRIP590 steel side (Fig. 10b).

Figure 11 shows the fracture morphologies of the tensile specimens of welded joints under 160 J mm^{-1}. Before magnetic field application, the fracture location of the welded joint is located in the coarse grain zone on the side of TRIP590 steel, the dimples on the joint fracture surface are sparse and shallow, while a few

zones exhibit a quasi-cleavage fracture morphology, indicating that the coarse-grain zone on the TRIP590 steel has poor plasticity, as shown in Fig. 11a. After magnetic field application, due to the concentration of heat energy, the fracture locations of the tensile specimens are at the TRIP590 base metal. The number of dimples on the fracture surface of the base metal is significantly increased, and the dimples are deeper. Moreover, there is no cleavage fracture morphology, as shown in Fig. 11b. These results indicate that the plasticity of the welded joints is relatively better after magnetic field application.

Hence, under the synergistic effects of appropriate magnetic field parameters and heat input, a fine crystal microstructure with desirable strength and plasticity can be generated in the coarse-grain zones, which is particularly important for improving the mechanical properties of the joints.

4. Conclusions

In summary, the synergistic effects of adjusting the heat input level and applying a magnetic field on the microstructure and mechanical properties at various welding parameters were focused on during tailored laser welding of dissimilar metals, i.e., CP780 and TRIP590 steels. With the assistance of a magnetic field, the weld seams were regular and neat when the heat input range was 100–160 J mm^{-1}, and there were no splashes or obvious defects. The following conclusions can be drawn:

1. Before magnetic field application, the weld seam center is mainly composed of proeutectoid ferrite, acicular ferrite, granular bainite, and upper bainite, whereas the heat-affected zone on both sides is mainly composed of lath martensite and lower bainite. After magnetic field application, the continuous stirring effect of the thermoelectric force on the molten pool drives the internal convection movement of the molten pool, improves the cooling rate, and inhibits the ferrite transformation during the crystallization of the weld seam center. Consequently, the reaction process of the martensitic and bainite phase transitions is accelerated. Moreover, the laser energy can be concentrated, and the width of the welded joints decreases significantly. Therefore, lath martensite and lower bainite are generated in the weld seam center, and only martensite is generated in the heat-affected zone. The grain size in the heat-affected zone on both sides is reduced, and the softening degree of the heat-affected zone on the side of the CP780 steel is reduced. Consequently, the comprehensive mechanical properties of the welded joint are improved compared to those without magnetic field application.

2. With the increase of the heat input level, the effect of the steady-state magnetic field on the weld mi-

crostructure becomes stronger. When the heat input level exceeds $120\,\mathrm{J\,mm^{-1}}$, the stirring time of the thermoelectric magnetic force on the molten pool is prolonged, and the region of the martensitic and bainitic phase transitions in the weld seams is expanded.

3. Comprehensively speaking, among the eight testing groups, the mechanical properties of the welded joints under a heat input of $160\,\mathrm{J\,mm^{-1}}$ exhibit the most significant improvement with a magnetic induction intensity of $20\,\mathrm{mT}$. The yield strength and the average hardness values increase by 31.95 and 33.27 %, respectively, while the softening degree is further relieved compared to those without magnetic field application.

Acknowledgements

References

[1] Z. Wen, X. Jun, Advanced lightweight materials for automobiles: A review, Mater. Des. 221 (2022) 110994.
https://doi.org/10.1016/j.matdes.2022.110994

[2] H. Das, M. Mondal, S. T. Hong, Y. Lim, K.-J. Lee, Comparison of microstructural and mechanical properties of friction stir spot welded ultra-high strength dual phase and complex phase steels, Mater. Charact. 139 (2018) 428–436.
https://doi.org/10.1016/j.matchar.2018.03.022

[3] A. Milovanoff, L. Minet, L. Cheah, I. D. Posen, H. L. MacLean, R. Balasubramanian, Greenhouse gas emission mitigation pathways for urban passenger land transport under ambitious climate targets, Environmental Science & Technology 55 (2021) 8236–8246.
https://doi.org/10.1021/acs.est.0c06671

[4] W. Xu, D. Westerbaan, S. S. Nayak, D. L. Chen, F. Goodwin, Y. Zhou, Tensile and fatigue properties of fiber laser welded high strength low alloy and DP980 dual phase steel joints, Mater. Des. 43 (2013) 73–83.
https://doi.org/10.1016/j.matdes.2012.07.017

[5] W. Guo, L. Li, S. Dong, D. Crowther, A. Thompson, Comparison of microstructure and mechanical properties of ultra-narrow gap laser and gas-metal-arc welded S960 high strength steel, Optics and Lasers in Engineering 91 (2017) 1–15.
https://doi.org/10.1016/j.optlaseng.2016.11.011

[6] A. K. Sinha, D. Y. Kim, D. Ceglarek, Correlation analysis of the variation of weld seam and tensile strength in laser welding of galvanized steel, Optics and Lasers in Engineering 51 (2013) 1143–1152.
https://doi.org/10.1016/j.optlaseng.2013.04.012

[7] P. Švec, A. Schrek, M. Dománková, Microstructure evolution of fibre laser welded TRIP and HSLA steel sheets with different thicknesses, Kovove Mater. 57 (2019) 219–227.
https://doi.org/10.4149/km_2019_4_219

[8] T. Wang, M. Zhang, R. Liu, L. Zhang, Lin Lu, W.-H. Wu, Effect of welding speed on microstructure and mechanical properties of laser-welded transformation induced plasticity (TRIP) steels, J. Iron Steel Res. Int. 27 (2020) 1087–1098.
https://doi.org/10.1007/s42243-020-00397-x

[9] A. Grajcar, M. Morawiec, M. Różański, S. Stanob, Twin-spot laser welding of advanced high-strength multiphase microstructure steel, Opt. Laser Technol. 92 (2017) 52–61.
http://doi.org/10.1016/j.optlastec.2017.01.011

[10] N. Lun, D. C. Saha, A. Macwan, H. Pan, L. Wang, F. Goodwin, Y. Zhoul, Microstructure and mechanical properties of fibre laser welded medium manganese TRIP steel, Mater. Des. 131 (2017) 450–459.
https://doi.org/10.1016/j.matdes.2017.06.037

[11] K. Rahul, T. V. Rao, A. Keskar, H. N. Girish, P. Madhusudan, Investigation on the effect of power and velocity of laser beam welding on the butt weld joint on TRIP steel, J. Laser Appl. 32 (2020) 012016.
https://doi.org/10.2351/1.5133158

[12] M. Xia, Z. Tian, L. Zhao, Y. Norman Zhou, Metallurgical and mechanical properties of fusion zones of TRIP steels in laser welding, ISIJ International 48 (2008) 483–488.
https://doi.org/10.2355/isijinternational.48.483

[13] T. S. Gonçalves, G. L. de Faria, H. Mota de Siqueira, M. S. Fernandes de Lima, Weldability and mechanical behavior of laser-welded TRIP 750 steel sheets, Int. J. Adv. Manuf. Technol. 107 (2020) 2807–2815.
https://doi.org/10.1007/s00170-020-05223-y

[14] P. Švec, A. Schrek, M. Dománková, Microstructural characteristics of fibre laser welded joint of dual phase steel with complex phase steel, Kovove Mater. 56 (2018) 29–40. https://doi.org/10.4149/km_2018_1_29

[15] M. Morawiec, M. Różański, A. Grajcar, S. Stano, Effect of dual beam laser welding on microstructure-property relationships of hot-rolled complex phase steel sheets, Archives of Civil and Mechanical Engineering 17 (2017) 145–153.
https://doi.org/10.1016/j.acme.2016.09.007

[16] A. K. Pramanick, H. Das, J.-W. Lee, Y. Jung, H.-H. Cho, S.-T. Hong, M. Shome, A. K. Pramanick, Texture analysis and joint performance of laser-welded similar and dissimilar dual-phase and complex-phase ultra-high-strength steels, Mater. Charact. 174 (2021) 111035.
https://doi.org/10.1016/j.matchar.2021.111035

[17] Y. Najafi, F. Malek Ghaini, Y. Palizdar, S. Gholami Shiri, M. Pakniat, Microstructural characteristics of fusion zone in continuous wave fiber laser welded Nb-modified δ-TRIP steel, J. Mater. Res. Technol. 15 (2021) 3635–3646.
https://doi.org/10.1016/j.jmrt.2021.09.116

[18] Y. Wu, Y. Guo, W. Zhang, L. Li, Microstructure evolution and dynamic mechanical behavior of laser welded dissimilar joint between QP1180 and TRIP780, J. Mater. Res. Technol. 16 (2022) 977–987.
https://doi.org/10.1016/j.jmrt.2021.12.076

[19] E. Evin, M. Tomáš, The influence of laser welding on the mechanical properties of dual phase and trip steels, Metals 7 (2017) 239.
https://doi.org/10.3390/met7070239

[20] R. S. Sharma, P. Molian, Yb:YAG laser welding of TRIP780 steel with dual phase and mild steels for use in tailor welded blanks, Mater. Des. 30 (2009) 4146–4155. https://doi.org/10.1016/j.matdes.2009.04.033

[21] B. Chang, C. Allen, J. Blackburn, P. Hilton, D. Du, Fluid flow characteristics and porosity behavior in full penetration laser welding of a titanium alloy, Metall. Mater. Trans. B 46 (2015) 906–918.
https://doi.org/10.1007/s11663-014-0242-5

[22] F. Liu, H. Wang, X. Meng, C. Tan, B. Chen, X. Song, Effect of magnetic field orientation on suppressing porosity in steady-magnetic-field-assisted aluminum alloy deep-penetration laser welding, J. Mater. Process. Tech. 304 (2022) 117569.
https://doi.org/10.1016/j.jmatprotec.2022.117569

[23] F. Liu, B. Xu, K. Song, C. Tan, H. Zhao, G. Wang, B. Chen, X. Song et al., Improvement of penetration ability of heat source for 316 stainless steel welds produced by alternating magnetic field assisted laser-MIG hybrid welding, J. Mater. Process. Tech. 299 (2021) 117329.
https://doi.org/10.1016/j.jmatprotec.2021.117329

[24] R. Zhang, X. Tang, L. Xu, F. Lu, H. Cui, Mechanism study of thermal fluid flow and weld root hump suppression in full penetration laser welding of Al alloy with alternating magnetic field support, Int. J. Heat Mass Transfer 166 (2021) 120759.
https://doi.org/10.1016/j.ijheatmasstransfer.2020.120759

[25] L. Cao, Y. Yang, P. Jiang, Q. Zhou, G. Mi, Z. Gao, Y. Rong, Ch. Wang, Optimization of processing parameters of AISI 316L laser welding influenced by external magnetic field combining RBFNN and GA, Results Phys. 7 (2017) 1329–1338.
https://doi.org/10.1016/j.rinp.2017.03.029

[26] Q. Zhou, F. Zhang, X. Huang, Aggregate multiple radial basis function models for identifying promising process parameters in magnetic field assisted laser welding, J. Manuf. Process. 28 (2017) 21–32.
https://doi.org/10.1016/j.jmapro.2017.05.012

[27] C. Hu, C. Wang, X. Ma, Z. Zhu, P. Jiang, G. Mi, EBSD study on magnetic field altering crystal texture and grain growth during laser-hybrid welding, Mater. Des. 216 (2022) 110587.
https://doi.org/10.1016/j.matdes.2022.110587

[28] J. Chen, Y. Wei, X. Zhan, Q. Gao, D. Zhang, X. Gao, Influence of magnetic field orientation on molten pool dynamics during magnet-assisted laser butt welding of thick aluminum alloy plates, Opt. Laser Technol. 104 (2018) 148–158. https://doi.org/10.1016/j.optlastec.2018.02.020

[29] L. Cao, Q. Zhou, H. Liu, J. Li, S. Wang, Mechanism investigation of the influence of the magnetic field on the molten pool behavior during laser welding of aluminum alloy, Int. J. Heat Mass Transfer 162 (2020) 120390. https://doi.org/10.1016/j.ijheatmasstransfer.2020.120390

[30] M. Bachmann, V. Avilov, A. Gumenyuk, M. Rethmeier, Numerical assessment and experimental verification of the influence of the Hartmann effect in laser beam welding processes by steady magnetic fields, Int. J. Therm. Sci. 101 (2016) 24–34.
https://doi.org/10.1016/j.ijheatmasstransfer.2013.01.015

[31] V. V. Avilov, A. Gumenyuk, M. Lammers, M. Rethmeier, PA position full penetration high power laser beam welding of up to 30 mm thick AlMg3 plates using electromagnetic weld pool support, Sci. Technol. Weld. Join. 17 (2012) 128–133.
https://doi.org/10.1179/1362171811Y.0000000085

[32] V. V. Avilov, A. Fritzsche, M. Bachmann, A. Gumenyuk, M. Rethmeier, Full penetration laser beam welding of thick duplex steel plates with electromagnetic weld pool support, J. Laser Appl. 28 (2016) 022420. https://doi.org/10.2351/1.4944103

[33] M. Bachmann, V. Avilov, A. Gumenyuk, M. Rethmeier, About the influence of a steady magnetic field on weld pool dynamics in partial penetration high power laser beam welding of thick aluminium parts, Int. J. Heat Mass Transfer 60 (2013) 309–321.
https://doi.org/10.1016/j.ijheatmasstransfer.2013.01.015

[34] R. Chen, H. J. Kong, J. H. Luan, A. D. Wang, P. Jiang, C. T. Liu, Effect of external applied magnetic field on microstructures and mechanical properties of laser welding joint of medium-Mn nanostructured steel, J. Mater. Sci. Eng. A 792 (2020) 139787.
https://doi.org/10.1016/j.msea.2020.139787

[35] I. Kaldre, Y. Fautrelle, J. Etay, A. Bojarevics, L. Buligins, Influence on the macrosegregation of binary metallic alloys by thermoelectromagnetic convection and electromagnetic stirring combination, J. Cryst. Growth 402 (2014) 230–233.
https://doi.org/10.1016/j.jcrysgro.2014.06.029

[36] A. Lange, A. Cramer, E. Beyer, Thermoelectric currents in laser induced melts pools, J. Laser Appl. 21 (2009) 82–87. https://doi.org/10.2351/1.3120213

[37] X. Li, Y. Fautrelle, A. Gagnoud, D. Du, J. Wang, Z. Ren, N. Mangelinck-Noel, Effect of a weak transverse magnetic field on solidification structure during directional solidification, Acta Mater. 64 (2014) 367–381.
https://doi.org/10.1016/j.actamat.2013.10.050

[38] X. Chen, M. Luo, R. Hu, R. Li, L. Liang, S. Pang, Thermo-electromagnetic effect on weld microstructure in magnetically assisted laser welding of austenite steel, J. Manuf. Process. 41 (2019) 111–118.
https://doi.org/10.1016/j.jmapro.2019.03.033

[39] X. Chen, S. Pang, X. Shao, C. Wang, J. Xiao, P. Jiang, Three-dimensional transient thermoelectric currents in deep penetration laser welding of austenite stainless steel, Optics and Lasers in Engineering 91 (2017) 196–205. https://doi.org/10.1016/j.optlaseng.2016.12.001

[40] Y. Liu, Q. Sun, J. Liu, S. Wang, J. Feng, Effect of axial external magnetic field on cold metal transfer welds of aluminum alloy and stainless steel, Mater. Lett. 152 (2015) 29–31.
https://doi.org/10.1016/j.matlet.2015.03.077

[41] Y. Rong, J. Xu, T. Lei, Y. Huang, X. Shao, Ch. Wang, Magnetism aided mitigation of deformation and residual stress in dissimilar joint 316L with EH36, J. Mater. Process. Tech. 26 (2017) 339–406.
https://doi.org/10.1016/j.jmatprotec.2018.04.022

[42] X. Li, Y. Fautrelle, Z. M. Ren, Influence of thermoelectric effects on the solid-liquid interface shape and cellular morphology in the mushy zone during

the directional solidification of Al-Cu alloys under a magnetic field, Acta Mater. 55 (2007) 3803–3813.
https://doi.org/10.1016/j.actamat.2007.02.031

[43] X. N. Xu, Y. Tian, Q. B. Ye, R. D. K. Misra, Z. D. Wang, The significant impact of the characteristics of granular structure and granular bainite on the mechanisms contributing to strength-ductility combination, J. of Mater. Eng. and Perform. 30 (2021) 7479–7487.
https://doi.org/10.1007/s11665-021-05887-x

[44] Z. X. Qiao, Y. C. Liu, L. M. Yu, Z. M. Gao, Formation mechanism of granular bainite in a 30CrNi3MoV steel, Journal of Alloys and Compounds 475 (2009) 560–564.
https://doi.org/10.1016/j.jallcom.2008.07.110

[45] M. Düsing, R. Mahnken, A coupled phase field/diffusion model for upper and lower bainitic transformation, International Journal of Solids and Structures 135 (2018) 172–183.
https://doi.org/10.1016/j.ijsolstr.2017.11.018

[46] X. Wan, K. Wu, G. Huang, R. Wei, In situ observations of the formation of fine-grained mixed microstructures of acicular ferrite and bainite in the simulated coarse-grained heated-affected zone, Steel Research International 85 (2014) 243–250.
https://doi.org/10.1002/srin.201200313

[47] A. Lambert-Perlade, A. F. Gourgues, A. Pineau, Austenite to bainite phase transformation in the heat-affected zone of a high strength low alloy steel, Acta Materialia 52 (2004) 2337–2348.
https://doi.org/10.1016/j.actamat.2004.01.025